Powder Technology 379 (2021) 251–264

Contents lists available at ScienceDirect

Powder Technology

journal homepage: www.elsevier.com/locate/powtec

Three-dimensional Voronoi analysis of realistic grain packing: An XCT assisted set Voronoi tessellation framework

Changhui Zhang [a], Shiwei Zhao [a,b,*], Jidong Zhao [b], Xiaowen Zhou [a]

[a] State Key Laboratory of Subtropical Building Science, South China University of Technology, Guangzhou, China
[b] Department of Civil and Environmental Engineering, Hong Kong University of Science and Technology, Clearwater Bay, Kowloon, Hong Kong

ARTICLE INFO

Article history:
Received 26 June 2020
Received in revised form 28 September 2020
Accepted 15 October 2020
Available online 21 October 2020

Keywords:
3D reconstruction
Realistic grains
Packing structure
Voronoi tessellation

ABSTRACT

Voids play an important role in both transport properties and mechanical deformation of a granular material. It remains challenging to quantify void spatial distributions, especially in realistic granular packing with irregular grain shapes. This paper presents a three-dimensional (3D) framework for Voronoi analysis of realistic grain packing, based on a combination of modern X-ray computed tomography (XCT), quantitative image processing and computer simulation using the discrete element method (DEM). We also introduce an efficient and robust parallel processing tool, PySVT, based on Set Voronoi tessellation (SVT). 3D reconstruction of a realistic Ottawa sand assembly is conducted, and two numerical packings of ellipsoidal and spherical particles are generated to reproduce the structure of the realistic packing with the same grain size distribution and global void ratio (or porosity). A further comparison is made for a class of microstructural properties among these packings. For the solid (particle) phase, analyses of particle shape characteristics and contact network indicate statistically significant deviation occurs between 2D and 3D particle characteristics, in particular sphericity and roundness. The analyses for the void phase place an emphasis on the morphology of Voronoi cells and the local porosity. A log-normal distribution is found to describe well both the local porosity and the reduced surface area of Voronoi cells, which is in agreement with observations for numerical packings of non-realistic grains.

1. Introduction

Granular materials are commonly encountered in nature, industry, and engineering. The particulate arrangement (fabric) within a granulate matrix has been proven to exert a significant influence on the physical and mechanical behavior of a granular material [1–3]. For example, in soils mechanics, there are indeed some fundamental understandings of relationships between soil fabric and its mechanical behavior, but it remains a challenge to quantify soil fabric in the laboratory. Significant efforts have been focused on the two-dimensional (2D) quantification of fabric quantities of granular materials. For example, Oda [4] managed to quantify the local void ratio (porosity) distribution of sands from magnified 2D images in the early 1970s, which might be the first quantitative evidence of the influence of fabric on granular materials. Then in 1976, Oda [5] further introduced detailed examination of the relationship between the fabric of a granular assembly and its mechanical properties, where the image was divided into polygons enclosed by straight lines connecting the centers of gravity of the particles so that the area occupied by solid particles and voids can be measured manually for each polygon. However, the method of aforementioned Oda's approach to a large extent depends on the judgment of the operator when determining the centers of gravity of grains. Alternatively, Frost and Kuo [6] utilized a Cambridge Instruments Quantimet Q570 image analysis system to automatically calculate void ratios of sands. Nevertheless, one major limitation of these 2D investigations is that 2D sections of a granular material are adopted to abstract 3D statistical information, inevitably resulting in significant loss of accuracy. In addition, 2D observations on thin sections are usually destructive to the structure of the system. For example, the sliced profiles of two contacting particles are non-contacted in 2D. Hence, it is demanding to propose 3D scenarios to quantify realistic structures of particulate systems for further advancing the understanding of granular mechanics.

Over the past decades, the rapid advancements of high-resolution non-destructive imaging technologies, such as X-ray computed tomography and magnetic resonance imaging, have been applied to investigating the granular structure (e.g., Refs. [7–11]). With respect to numerical methods, particle-based numerical simulation tools, especially the discrete element method (DEM) [12], provide a direct way to observe and quantitatively measure grain-scale features and processes. Moreover, DEM can be used to generate packings by specifying the porosity or state-of-stress of the studied system, since particle external stresses and stress paths can be controlled (e.g., Refs. [13–15]).

* Corresponding author at: State Key Laboratory of Subtropical Building Science, South China University of Technology, Guangzhou, China.
E-mail addresses: ceswzhao@ust.hk, swzhao@scut.edu.cn (S. Zhao).

https://doi.org/10.1016/j.powtec.2020.10.054
0032-5910/

Particularly, the X-ray computed tomography (XCT) has been advantageously applied to quantifying geometrical properties of individual particles in both two and three dimensions. For instance, statistical methods based on spatial and image analyses have been also introduced to provide quantitative measures on volume, surface area, curvature and connectivity of particles [16]. Furthermore, XCT shows its potential in obtaining internal and microstructure details, e.g., porosity [17,18], and pore network [19–21], biomass distribution, bulk density, soil organic matter distribution, and transport parameters [22–25]. Hence, it is possible to extract realistic pore networks of grain packings or any other porous media [19,26,27] and investigate the local void ratio evolution of granular materials, which reflects the heterogeneity and anisotropy of a packing [28]. However, it remains a challenge to quantify the spatial characteristics of an entire network of the pore. As a workaround, the entire space occupied by both grains and pores is partitioned into a gap-free and non-overlapping pattern of cells. The prevailing approaches in partition are Delaunay triangulation and Voronoi tessellation, which provide dual patterns of partition. Delaunay tessellation has void space shared by a set of particles, while Voronoi tessellation associates void space to every single particle.

Remarkably, Voronoi tessellation can reproduce the anisotropy of local particle distribution. The Voronoi-tessellation-based geometry has also been employed in building the statistical mechanics theory for granular packings [29]. Nevertheless, such kind of analysis has been commonly conducted for sphere packings [30,31] or ellipsoid packings [28,32]. For instance, Schaller et al. [33] reported a Voronoi analysis of the packing of monosized frictional ellipsoids and demonstrated that the local packing fraction distribution can be correlated with the overall packing fraction. Schröder-Turk et al. [34] utilized Minkowski tensors to quantify the characteristics of 3D sphere packing in conjunction with a Voronoi tessellation. Recently, Zhao et al. [35] explored the universal characteristics in sheared granular materials composed of poly-superellipsoidal particles by using the Set Voronoi tessellation. These aforementioned studies mainly focused on the geometric characteristics and anisotropies of Voronoi cells of particles with analytical shapes, while there have been few reports on the Voronoi analysis of packings composed of complex realistic grains.

In this study, we present a novel framework of Voronoi analysis of realistic grain packing reconstructed from X-ray computed tomography (XCT) images. For the completeness of the presentation, a route of 3D reconstruction of realistic grain assembly with the critical image processing algorithms is introduced in Section 2. With regard to the pore network structure, three possible schemes of Voronoi tessellation (ordinary Voronoi tessellation, radical Voronoi tessellation, and Set Voronoi tessellation) are summarized in Section 3, where we propose an efficient and robust tool for the Set Voronoi tessellation of realistic grain packings. With the proposed framework, we analyze three particulate systems composed of realistic sands, spheres, and ellipsoids, respectively, as a demonstration. The corresponding results are presented and discussed in Section 4, in which physical characteristics (including particle size distribution, particle shape characteristics and interparticle contacts) and morphological properties of Voronoi cells of the three packings are examined and discussed at the microscopic scale. In addition, a parametric analysis of Voronoi cells is carried out as well.

2. 3D reconstruction of realistic grain assembly

2.1. X-ray projection and sand assembly

A natural sand assembly (Ottawa-20/30, standard sand in the geotechnical laboratory) was prepared for imaging and subsequent Voronoi analysis. Sand particles were poured into a container with a dimension of 12.20 mm × 12.20 mm × 16.80 mm, followed by a scanning process of a phoenix X-ray computed tomographer with an X-ray tube voltage of 150 kV and a current of 80 μA, which yields 1531 stacks of images with a resolution of 11 μm per pixel. A schematic diagram of the acquisition process is shown in Fig. 1. The X-ray scan process outputs a back-projected image that is a spatial reconstruction of the attenuation coefficients based on integral linear projections [36]. With a sequence of projections (32-bit 2D cross-sections), it is straightforward to obtain the corresponding 8-bit gray-scale images for further segmentation. Although the captured image is a mapping of the material density under observation, it does not allow us to completely distinguish between particles in the packed bed. Hence, image segmentation is performed by a sequential image processing essentially as briefly depicted in the following sections. Fig. 2 presents the flow chart of the image processing and analysis procedure on the projection images. Interested readers are referred to the literature, e.g., Ref. [37], and among others, for more details on image processing.

2.2. 3D reconstruction of sand assembly

In the presence of digital noise, the subsequent image processing may yield unexpected results, especially in the watershed segmentation. Hence, a 3D median filter with a dimension of 3 × 3 × 3 (voxels) is first implemented as a low-pass filter in order to reduce the random noise. Thresholding is then performed to segment the foreground (i.e. solid particle phase) from the background (i.e. void or pore phase) to obtain a binary image for each single CT slice, as shown in Fig. 4(b). The threshold value is determined by the intensity histogram of the images based on Otsu's threshold method [38]. The above image processing procedures are implemented in an extension of ImageJ [39] along with supplementary plugins such as *3D Watershed Segmentation* in Java (programming language).

Segmentation is one of the most critical steps in the process of reducing images to more useful information [37]. In our particular case, the 3D watershed segmentation method is chosen to identify separate geographical catchment basins based on the downhill flow of water to local low points. Fig. 3 gives an example of distance transformation for two touching particles. The key point of the segmentation process is to find markers and locations of the particles [40]. A 3D distance map can be built where a binary image is mapped to the image that specifies the distance from each pixel to the nearest non-zero pixel. Once the markers are defined, the process to label the particles with an index is carried out using the flooding model, then an identification number is assigned to each particle. The image processing workflow for a successful volume segmentation using a marker-controlled watershed transformation of two connected objects is shown in Fig. 4. As a result of the high resolution and clarity of CT images, the 3D voxel representation of particles captures morphology very well. Finally, a widely used surface reconstruction method, Screened Poisson Reconstruction [41], is then applied to creating smooth and watertight surfaces based on surface voxels.

3. Voronoi tessellation

3.1. Ordinary Voronoi tessellation

Voronoi tessellation is originally proposed to tessellate a domain including a given collection of points rather than spheres with sizes, as illustrated in Fig. 5 for a two-dimensional case. Given a number of points (called seeds) $\mathbf{P} = \{\boldsymbol{p}_1, \boldsymbol{p}_2, \ldots, \boldsymbol{p}_n\}$ in a domain Ω, for each point, its corresponding Voronoi cell is defined as the region that consists of all points closer to it that to any others, so that the entire space is partitioned among these points. Mathematically, the ith Voronoi cell C_i is defined as

$$\mathrm{C}_i = \left\{ \boldsymbol{x} \in \Omega \,|\, \|\boldsymbol{x} - \boldsymbol{p}_i\| = \min_{j=1} \|\boldsymbol{x} - \boldsymbol{p}_j\| \right\}, i = 1, 2, \ldots, N_p \quad (1)$$

where $\boldsymbol{x}$ is an arbitrary point in the domain; N_p is the number of points in $\mathbf{P}$; $\|\cdot\|$ denotes the Euclidean distance. Thus, the entire domain is

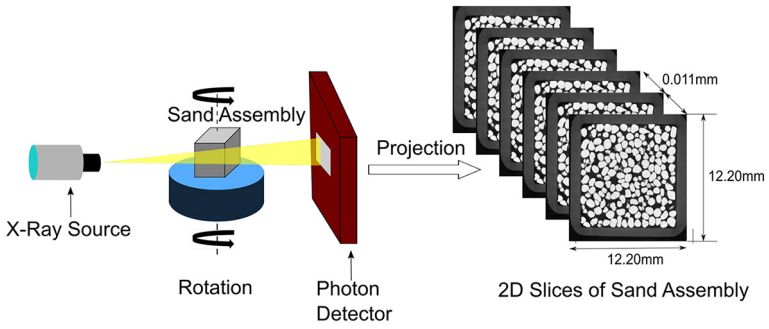

Fig. 1. Schematic diagram for the data acquisition process.

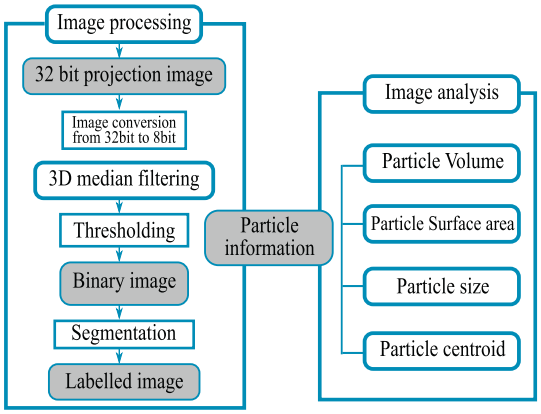

Fig. 2. Flow chart of image processing and analysis of X-ray CT images.

composed of all cells $\mathbb{C} = \{\boldsymbol{C}_1, \boldsymbol{C}_2, \ldots, \boldsymbol{C}_{N_p}\}$ that are a series of convex and non-overlapping cells bounded by planar surfaces. Each face of Voronoi cells is derived from the planes bisecting and perpendicular to the vectors connected by points, while the edges of cells are formed by the intersection of these planes. Hence, in the ordinary Voronoi tessellation technique, only the neighboring points are the necessary information to construct a Voronoi cell, implying that a limited subdomain needs searching.

3.2. Radical Voronoi tessellation

A prevailing extension of Voronoi tessellation, i.e., *radical Voronoi tessellation*, also known as *Laguerre Voronoi tessellation* [42], helps to impose the size of each cell via the introduction of a local radius r for each seed point. Given a set of N_p seed points $\mathbf{P} = \{\boldsymbol{p}_1, \boldsymbol{p}_2, \ldots, \boldsymbol{p}_n\}$ with radii of $r_1, r_2, \ldots, r_n$, respectively, a Voronoi cell C_i is expressed as

$$\mathrm{C}_i = \left\{ \boldsymbol{x} \in \Omega | d(\boldsymbol{x}, \boldsymbol{p}_i, r_i) = \min_{k=1} \{ d(\boldsymbol{x}, \boldsymbol{p}_k, r_k) \} \right\}, i = 1, 2, \ldots, N_p \tag{2}$$

where $d(\boldsymbol{x}, \boldsymbol{p}_i, r_i)$ denotes the Euclidean distance between the geometrical surface of $\boldsymbol{p}_i$ and a point $\boldsymbol{x}$, i.e.,

$$d(\boldsymbol{x}, \boldsymbol{p}_i, r_i) = \sqrt{\|\boldsymbol{x} - \boldsymbol{p}_i\|^2 - r_i^2} \tag{3}$$

Similar to the ordinary Voronoi tessellation, the radical Voronoi tessellation partitions the entire packing space into a set of non-overlapping convex polyhedra, where each polyhedron encloses a single particle, as shown in Fig. 6(a). The separate plane between two neighboring particles is the set of points with equal tangential distance to the two spheres, rather than the bisecting plane. Thus, the polyhedron face as part of the plane is guaranteed to be outside the particles and will not intersect with any particles. The radical Voronoi tessellation retains most of the features of the ordinary Voronoi tessellation, and it recovers the Voronoi bisecting plane for mono-disperse particles.

3.3. Set Voronoi tessellation

Radical Voronoi diagrams are defined with reference to the center of the particles (i.e., distinct points), thereby only suitable for systems of spherical particles including both mono-disperse and poly-disperse spheres. For non-spherical particles, however, Voronoi diagrams based on the particle centers cannot be carried out directly. To address this issue, we introduce an alternative approach *Set Voronoi tessellation* proposed by Schaller et al. [43], which constructs Voronoi cells on the basis of boundary surfaces of the particle rather than that of the particle center. One important step of Set Voronoi tessellation is to discretize the

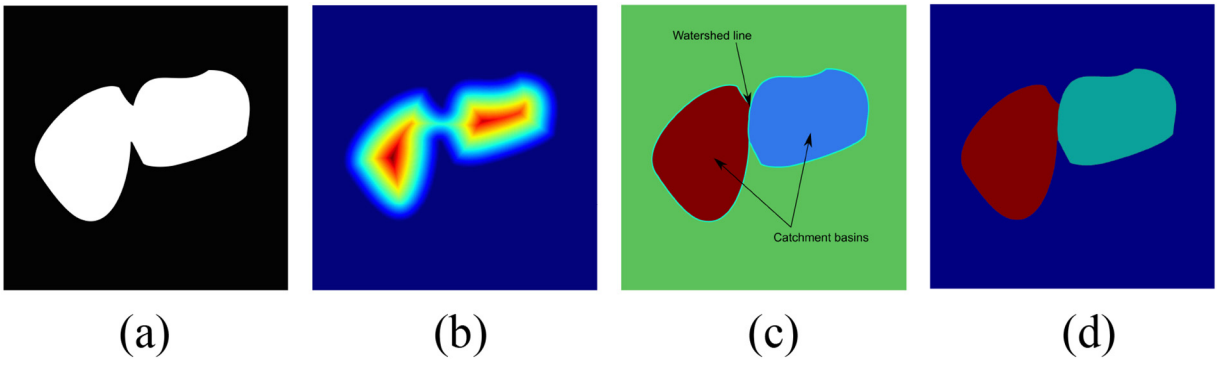

Fig. 3. Extraction and identification of individual particles: (a) CT binary image of two touched particles, (b) distance transformation of the two particles, (c) watershed line and catchment basins of the two particles and (d) two labeled individual particles.

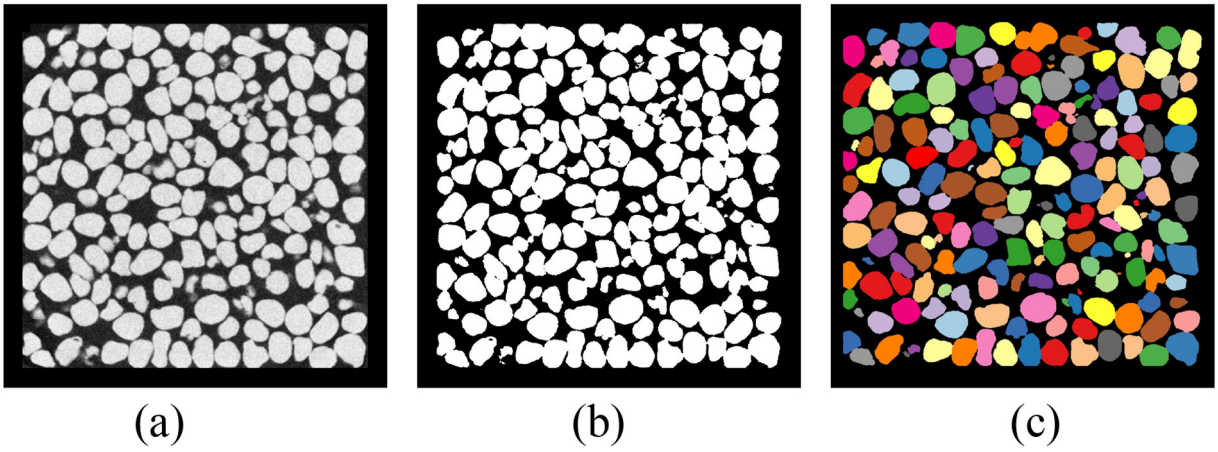

Fig. 4. Image processing on a typical CT slice: (a) original CT gray-scale image, (b) binary image after thresholding and (c) labeled image.

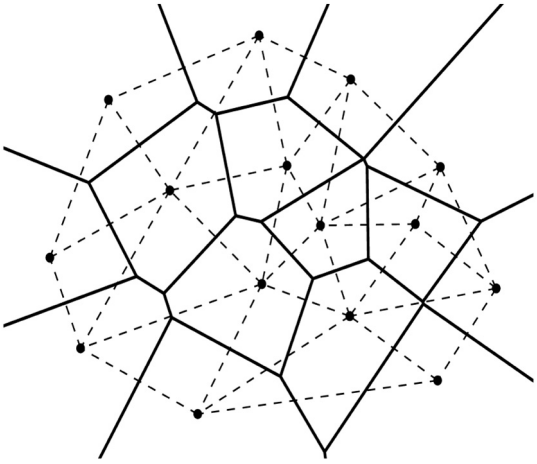

Fig. 5. Two dimensional illustration of an ordinary Voronoi diagram (solid) for a given set of points in the plane and the dual Delaunay triangles (dashed).

bounding surface of all particles in the domain into a sufficiently dense set of vertices and then compute Voronoi diagrams of all these distinct vertices by means of the ordinary Voronoi tessellation as mentioned above. The Set Voronoi cell of each particle P_i is constructed by uniting all these Voronoi cells of the vertices on the bounding surface of P_i.

Theoretically, given a set of N_p particles **P** in a 3D Euclidean space $\mathbb{R}^3$, the bounding surface of particle P_i is denoted by $S_i = \partial P_i$, and the Set Voronoi cell C_i is defined as the region of space closer to the bounding surface S_i of particle P_i than to any other particle P_j $(i \neq j)$, i.e.,

$$C_i = \left\{ \boldsymbol{x} \in \mathbb{R}^3 | d(\boldsymbol{x}, S_i) = \min_{k=1} \{ d(\boldsymbol{x}, S_i) \}, S_i = \partial P_i \right\} \tag{4}$$

Note that the distance between a point $\boldsymbol{x}$ and the ith particle are calculated from the point **x** to the nearest point on the bounding surface of the particle, rather than to its center, referring to Fig. 6(b). Additionally, the definition of particle P_i for *Set Voronoi tessellation* is valid for not only convex but also non-convex shapes, since the discretization process of each particle is employed and three dimensional *Point Voronoi Tessellation* is adopted afterwards. Particles are fully enclosed by their Set Voronoi cells, implying that the Set Voronoi cells may have curved surfaces (see e.g. the Voronoi surface of particle P_2 in Fig. 6(b)), and their shapes may be non-convex even for convex particles (e.g., particle P_3 in Fig. 6(b)).

3.4. Surface sampling algorithm

With respect to Set Voronoi tessellation, points belonging to the particle surfaces are of our primary interest. Hence, it may be essential to generate uniformly distributed points from reconstructed particle

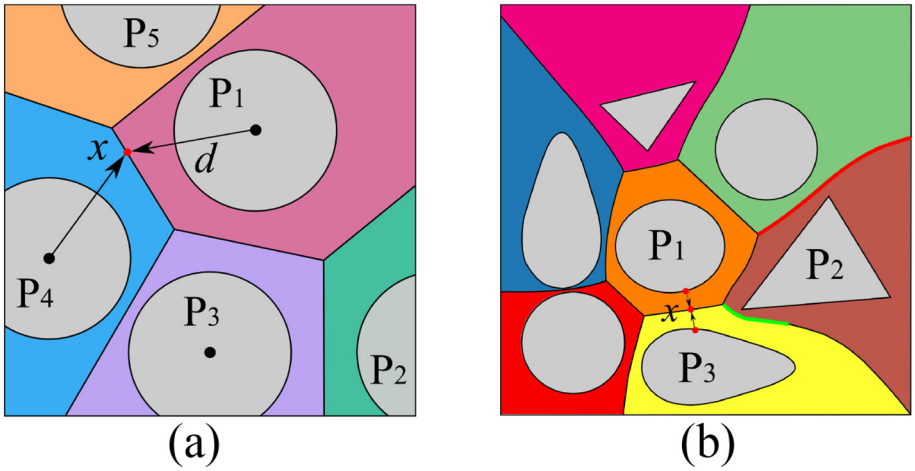

Fig. 6. A representation of Voronoi diagram a system of mono-disperse spheres (a), and the Set Voronoi diagram of a mixture of differently shaped objects (b).

surfaces. Many effective surface sampling algorithms have been proposed, such as Monte Carlo Sampling, Regular Recursive Sampling and Poisson-disk Sampling [44–46]. In this study, Poisson-disk Sampling algorithm is introduced. Given a reconstructed surface, this algorithm computes a set of samples that are randomly distributed on the surface, and the samples are at least a minimum distance away from each other. One advantage of this method is that it is capable of generating a target number of surface points by controlling the minimum distance of samples. For a detailed description of this method, readers are referred to Refs. [46–48].

3.5. A parallel processing tool for set Voronoi tessellation

A parallel processing tool, PySVT, for Set Voronoi tessellation (SVT) is proposed in a hybrid programming of C++ and Python. The tool implements SVT of discrete surface points generated from poly-superellipsoids or other irregular particles utilizing the Voro++ library [49]. For brevity, we summarize major processing steps as follows:

(1) Initialization: After obtaining spatially discrete particle surface points, Python script provides an interface to parse particle information and global boundary conditions.
(2) Neighbor search: For efficiency, it is acceptable to assume the Set Voronoi cell of given particle P_i is rather affected by the nearer neighbors of particle P_i than by more distant particles. Therefore, a neighbor list is built for particle P_i by searching for adjacency particles within a distance R_s.
(3) AABB enlargement: A strategy is introduced to take into account all possible surface points of neighboring particles, where the axis-aligned bounding box (AABB) of particle P_i is enlarged in all dimensions with a scaling coefficient, Φ. The surface points of neighboring particles enclosed in the enlarged AABB are then prepared for point Voronoi tessellation, as illustrated in Fig. 7. Moreover, the boundary of the intersection between the enlarged AABB and the global container is taken as the local computational domain. Note that the scaling coefficient, Φ might have an influence on the SVT results, which will be discussed in the following section.
(4) Parallel SVT: OpenMP is used for multi-threaded parallelism on each particle with the purpose of taking full advantage of CPUs and improving the speed of SVT processing. The assembly can therefore be tessellated for multiple particles simultaneously and independently.
(5) Post-processing: Finally, a triangulated representation of constructed Set Voronoi cells is obtained, and corresponding properties (e.g. cell surface area and volume) will be exported. It is worth noting that the Voronoi cells are irregular polyhedrons which are far more complicated than the enclosed particles. Both cell surface area and volume are calculated by summing up all corresponding surface areas and volumes of the point Voronoi cells from the particle surface points, respectively. More details are depicted in our previous work [28].

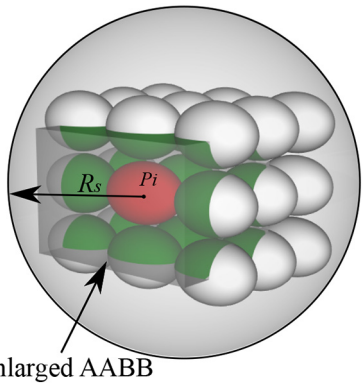

Fig. 7. An exemplified local computational domain of particle P_i with an enlarged AABB.

4. Results and discussion

4.1. Realistic and numerical packings

A packing of Ottawa 20–30 sands with 3092 particles is reconstructed following the procedure outlined in Section 2, as shown in Fig. 8(a). The global porosity of this realistic packing is 0.578. To explore microscopic characteristics of different systems and validate the applicability of SVT, two more DEM packings composed of spheres and ellipsoids are prepared using an open-source DEM code, SudoDEM (https://sudodem.github.io) [13,50,51,70]. Both packings have identical dimensions along x- and y-axes (equal to 10 mm), while the height of packings is set up to control packings' porosity. The porosity of both numerical packings is equal to that of the reconstructed sand assembly. The detailed protocol of packing generation is depicted as follows. In the initial configuration, the sand particles in the reconstructed packing are replaced by equal-volume spheres or ellipsoids one-by-one with the same positions. Note that the aspect ratios of ellipsoids are consistent with that of the corresponding sand particles. By doing so, it is not surprising to see overlapping particles at the above configuration. Hence, it is essential to constrain the displacement of particles to avoid excessive initial velocities of particles within certain time steps during DEM cycling. Then, particles are unleashed to settle down freely under gravity until reaching a relative equilibrium state, e.g., the unbalanced force ratio below a threshold (e.g., 1×10^{-5}). After that, the top wall moves downwards slowly with packing porosity approaching to that of the sand packing such that the stress exerted on the top wall keeps much less than (<5%) the gravity on the bottom wall. The values of major parameters in the DEM simulations are selected in experience [13] and listed in Table 1. Four side walls of the numerical packings are assumed frictionless, while the coefficient of friction between particles and the bottom wall is set to 1.0. Fig. 8 shows the snapshots of the configurations for the three packing with reconstructed sands, spheres and ellipsoids.

4.2. Voronoi parametric analysis

4.2.1. Effect of AABB scaling coefficient

Remarkably, it is sufficient to carry out SVT in an enlarged AABB of particle P_i in most cases. Nevertheless, it remains difficult to determine the extent of the enlarged AABB. To address this problem, we select 148 particles of the sand assembly with diameter distribution near D_{50} (i.e. 0.74 mm) to investigate the effect of the AABB scaling coefficient Φ on the number of neighboring particles, Set Voronoi cell volume and surface area.

As expected, the average number of particles contained in AABB increases dramatically with the scaling coefficient, as shown in Fig. 9(a), implying that the enlargement of local computational domain requires more computing resources for an individual particle accordingly. Hence, the accuracy of SVT computation is further examined. Quantitatively, a relative error E_R under two adjacent Φs is introduced to evaluate the variation of cell volume or surface area, given by

$$E_R = \left|\frac{V_{\Phi_i} - V_{\Phi_j}}{V_{\Phi_i}}\right| \quad or \quad E_R = \left|\frac{S_{\Phi_i} - S_{\Phi_j}}{S_{\Phi_i}}\right| \tag{5}$$

where V and S refer to cell volume and surface area, respectively; the subscripts Φ_i and Φ_j denote scaling coefficients identical to i and j, respectively. With different scaling coefficients ranging from 2.0 to 5.0, the average relative errors of cell volume and surface area of 148 particles are calculated. As shown in Fig. 9(b), the average relative errors of cell volume and surface area decrease evidently as the scaling

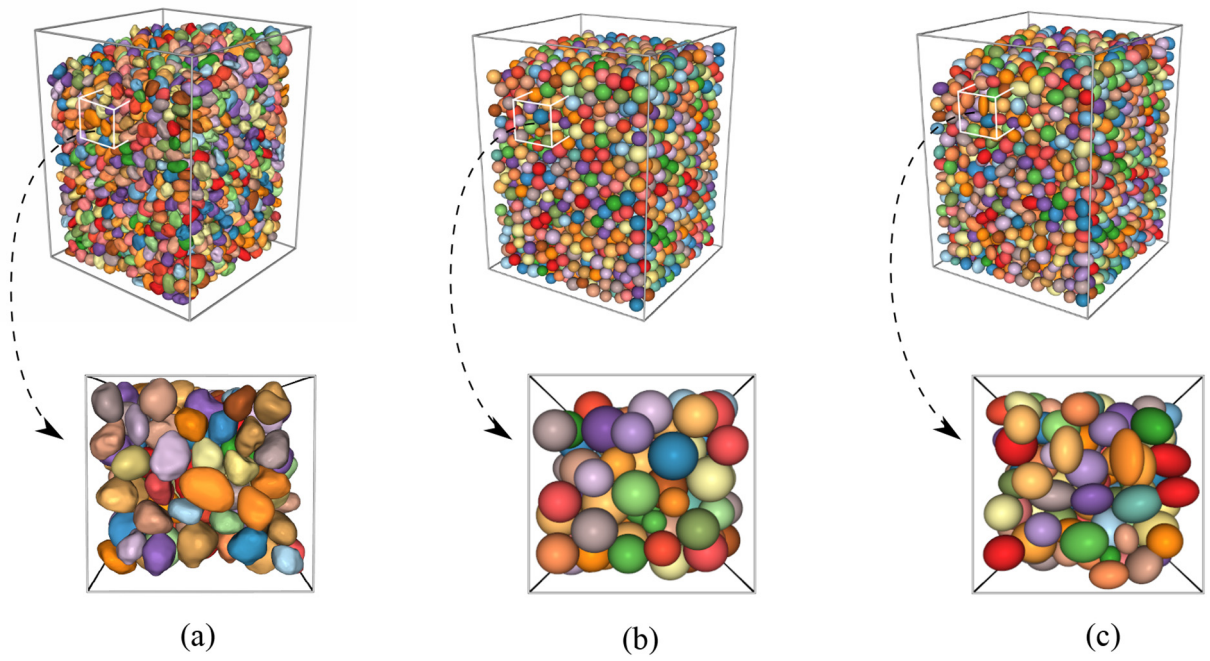

Fig. 8. Packs of 3092 particles with identical porosity using different particles: (a) reconstructed sands, (b) spheres and (c) ellipsoids.

Table 1
Major parameters used in the DEM simulations.

Simulation parameter	Value
Particle density, $\rho(kg/m^3)$	2650
Particle coefficient of friction, μ	0.5
Damping coefficient, α	0.3
Particle/wall normal stiffness, $K_n(N/m)$	1×10^8
Particle/wall tangential stiffness, $K_t(N/m)$	7×10^7

coefficient increases. Furthermore, cell volume and surface area change slightly with average E_R smaller than 0.1% when the scaling coefficient is greater than 4. It implies that the corresponding Voronoi cell converges and tends to be more accurate if the constructed local computational domain is sufficiently large.

4.2.2. Voronoi resolution

It is essential to produce spatially discrete surface points for SVT in the first place. For XCT scanned sands, a sampling algorithm is employed to generate point clouds from the reconstructed particle surfaces. However, with a reconstructed particle surface, it is not clear that how many points are sufficient to guarantee the accuracy of SVT computation. The influence of the number of surface points (i.e., resolution) on the accuracy of both volume and surface area of Voronoi cells is thus evaluated.

As shown in Fig. 10, it can be seen that there is no significant difference in both volume and surface area of Voronoi cells between Resolution 2000 and other higher resolutions, whilst one sees a clear deviation between Resolution 800 and the other resolutions. The reason is that Set Voronoi cell has more noise in a lower resolution [28]. Therefore, a trade-off between accuracy and computational cost is performed. A local domain consisting of approximately 60 particles is adequately

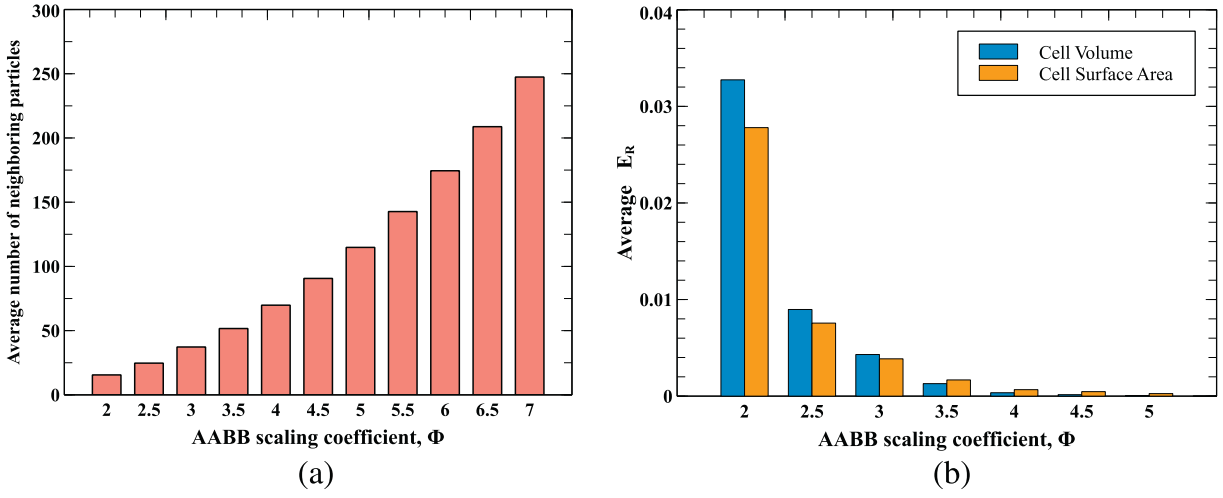

Fig. 9. The influence of neighbor search radius on the average number of neighboring particles, Voronoi cell volume and surface area: (a) average number of neighboring particles, (b) cell volume and surface area.

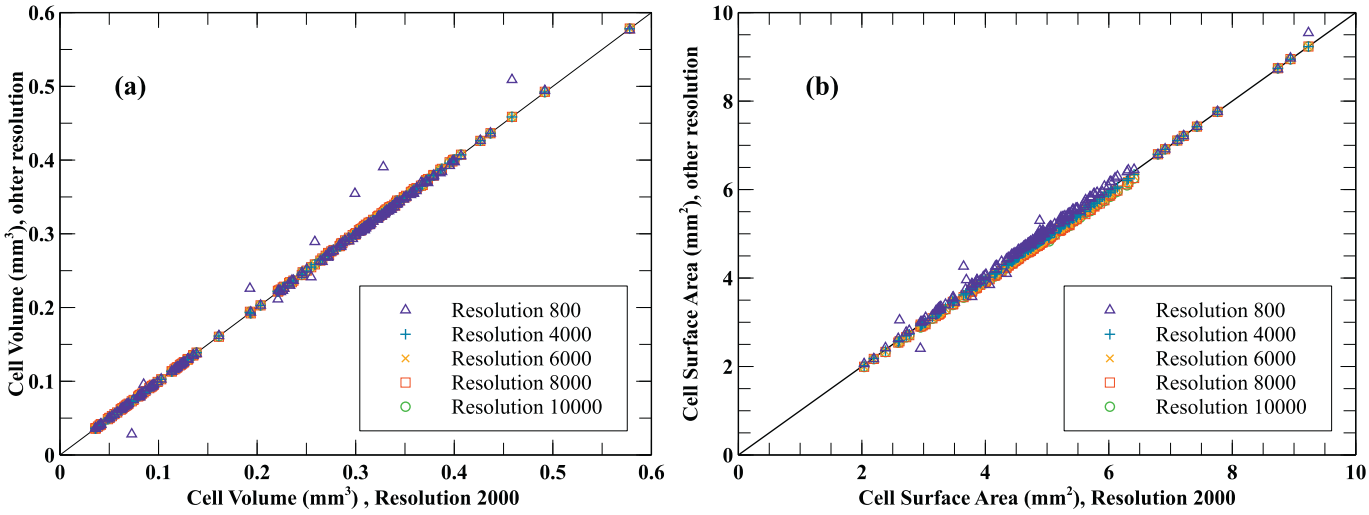

Fig. 10. The volume and surface area of Set Voronoi cells with different resolutions: (a) cell volume and (b) cell surface area.

large for realistic sands, which corresponds to an AABB scaling coefficient of 4. Moreover, a reasonable resolution of XCT-reconstructed particles is well capable of performing SVT, and Resolution 2000 is selected for the subsequent analyses.

4.3. Particulate analysis

4.3.1. Particle size distribution

Particle size distribution (PSD) is one of the most fundamental and important properties of granular materials, which can be obtained by mechanical sieving tests at the laboratory. In sieve analysis, the particle size is quantified by the minimum size of sieve aperture through which the particle can pass. In this work, the following equivalent sphere diameter D of the volume of particles is employed due to its wide application in laser particle size analysis [52,53]

$$D = \left(\frac{6}{\pi} V_p\right)^{1/3} \tag{6}$$

where V_p is the particle volume. Compared with the sieve analysis method, the advantage of analytical particle size lies in its repeatability and flexibility. For example, characterization of the granular packing provides details on the grain size distribution, which helps to observe the evolution of particle size within crushable granular materials subjected to loadings. Moreover, the equivalent spherical diameter has been not only employed for particles with moderate distortion in shape from sphere but also for irregular particles, even for star-shaped particles [54]. There might be more elegant definitions of particle size for non-spherical particles, which is, however, beyond the scope of this study.

Principal component analysis (PCA) is employed to determined the major (long), intermediate, and minor axis orientations of each particle. Using this orientation data an orthogonal rotation is applied and each particle is rotated so that its principal axes were parallel to the Cartesian axes. The major (a), intermediate (b) and minor (c) dimensions of the particle are then taken to be $a = \max(x') - \min(x')$, $b = \max(y') - \min(y')$ and $c = \max(z') - \min(z')$, where x', y', z' are 1D arrays giving the particle's voxel coordinates following rotation. Note that the center of gravity (x_0, y_0, z_0) and the moment of inertial matrix ($\mathbf{I}$) are given by Eq. (7) and Eq. (8) respectively.

$$x_0 = \frac{\sum_i x_i}{N_v}, y_0 = \frac{\sum_j y_j}{N_v}, z_0 = \frac{\sum_k z_k}{N_v} \tag{7}$$

$$\mathbf{I} = \begin{bmatrix} I_{xx} & -I_{xy} & -I_{xz} \\ -I_{yx} & I_{yy} & -I_{yz} \\ -I_{zx} & -I_{zy} & I_{zz} \end{bmatrix} \tag{8}$$

where N_v denotes the number of voxels that make up the particle, and

$$I_{xx} = \sum_j \left(y_j - y_0\right)^2 + \sum_k (z_k - z_0)^2 \tag{9a}$$

$$I_{yy} = \sum_i (x_i - x_0)^2 + \sum_k (z_k - z_0)^2 \tag{9b}$$

$$I_{zz} = \sum_i (x_i - x_0)^2 + \sum_j \left(y_j - y_0\right)^2 \tag{9c}$$

$$I_{xy} = I_{yx} = \sum_i (x_i - x_0) \sum_j \left(y_j - y_0\right) \tag{9d}$$

$$I_{xz} = I_{zx} = \sum_i (x_i - x_0) \sum_k (z_k - z_0) \tag{9e}$$

$$I_{yz} = I_{zy} = \sum_j \left(y_j - y_0\right) \sum_k (z_k - z_0) \tag{9f}$$

Fig. 11 illustrates the principal directions of a particle composed of 230535 voxels. The cumulative distribution of three principal axes lengths and particle diameters D of the XCT-reconstructed sands are plotted in Fig. 12(a). It can be seen that the curve of volume-equivalent diameter D situates between the curves of intermediate length and minor length. Besides, the experimental data is almost on the analytical curve of D, suggesting that the equivalent-volume approach is applicable to quantifying the PSD of Ottawa 20–30 sand. The histogram of particle size distribution of the volume-equivalent diameter is plotted in Fig. 12(b), which shows a normal distribution with sizes mostly between 650 and 850 μm.

4.3.2. Particle shape characteristics

It remains a challenge to fully characterize particle morphology, especially for realistic complex particle shapes. Indeed, it is well-acknowledged that the complex particle shape can not be fully captured by a single descriptor. Nevertheless, a combination of several shape descriptors may correlate better with a given mechanical characteristic of a granular material. Blott and Pye [55] showed that the most important aspects of particle shape can be characterized by using parameters representing the form (e.g., sphericity), roundness (or angularity) and

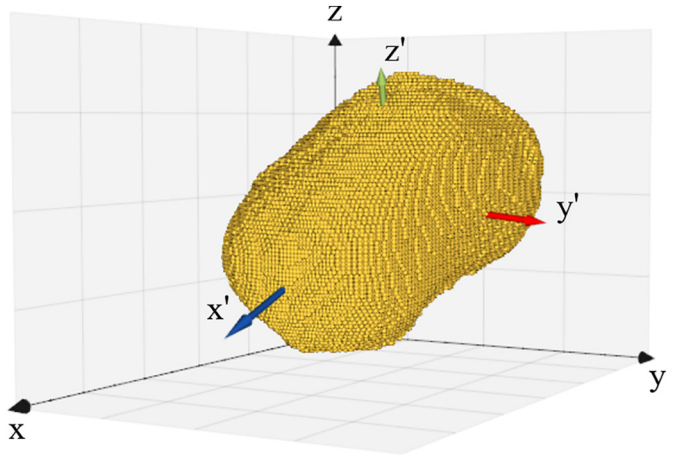

Fig. 11. Illustration of a particle composed of 230505 voxels and the corresponding principal directions $x'y'z'$ in the global coordinate system xyz.

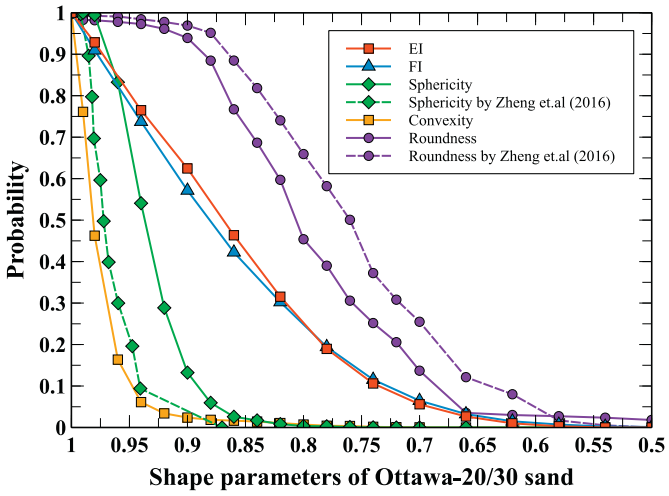

Fig. 13. Cumulative distributions of shape parameters for Ottawa-20/30 sand.

irregularity (e.g., convexity). With the reconstructed Ottawa 20–30 sand packing, we analyze the particle morphology with a focus on four common shape descriptors including aspect ratio, sphericity, roundness, and convexity, as depicted below.

As for aspect ratio, the elongation index (EI) and the flatness index (FI) are calculated based on the principal dimensions, given by Eq. (10a) and Eq. (10b), respectively.

$$\mathrm{EI} = b/a \tag{10a}$$

$$\mathrm{FI} = c/b \tag{10b}$$

where a, b, c are three principal dimensions introduced above. Moreover, sphericity Ψ, defined as Eq. (11a), is adopted to describe the overall form of the particle irrespective of the sharpness of edges and corners, thereby quantifying the degree of conformity of particle shape to that of a sphere. Another measure to compute the compactness is convexity, C_x, defined as the ratio of the particle to the volume of the convex hull enclosing the particle, given in Eq. (11b). Following the definition by Wadell [56], roundness $\mathscr{R}$ is defined as the ratio of the average radius of curvature of the corners of the particle's silhouette to the radius of the maximum inscribed sphere. Note that although roundness is a 3D property, some approaches work with the maximum 2D projection plane (silhouette) of the particle looking for a trade-off between accuracy and efficiency, e.g., Zheng et al. [57]. In the present work, we evaluate area-based average roundness [58] by calculating the surface mean curvatures based on the 3D surface coordinates and triangulated mesh, given by Eq. (11c), since the local determination of roughness is beyond the scope of this paper.

$$\Psi = \frac{\left(36\pi V_p^2\right)^{\frac{1}{3}}}{S_p} \tag{11a}$$

$$C_x = V_p / V_{CH} \tag{11b}$$

$$\mathscr{R} = \frac{\sum\left(A_n \frac{k_{ins}}{k_M}\right)}{\sum(A_n)} \tag{11c}$$

where S_p refers to the surface area of a particle, and V_{CH} denotes the volume of the convex hull enclosing the particle; k_{ins} and k_M are the curvature of the maximum inscribed sphere and the mean curvature of the particle, respectively; and A_n is the area of the nth triangular facet.

Fig. 13 shows the cumulative distributions of shape parameters for Ottawa-20/30 sand particles, where the results from Zheng et al. [57] are plotted together for a comparison. Note that the shape parameters are measured with full projections (2D) from the assemblies in Zheng et al. [57]. Besides, the mean values of these shape parameters are listed in Table 2. As can be seen in Fig. 13, the distributions of the elongation index (EI) and the flatness (FI) are almost superimposed in 3D measurement, which is not surprising due to the equivalent physical meaning of

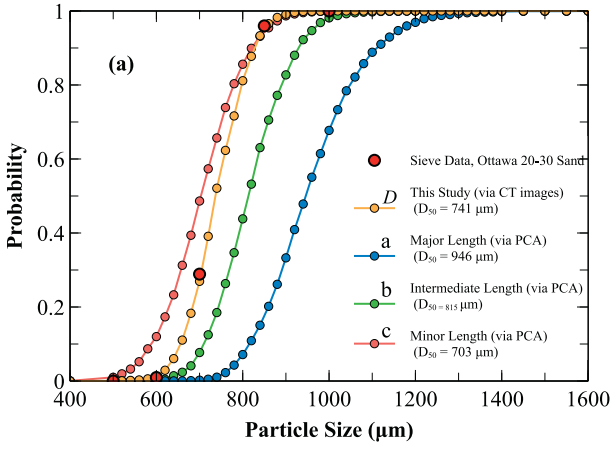

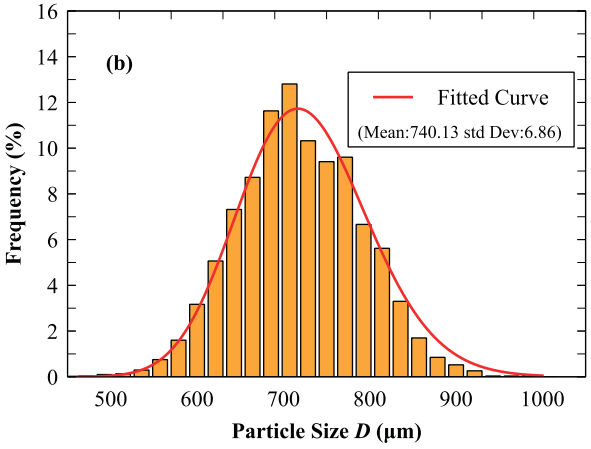

Fig. 12. (a) Particle size distribution of 3092 particles based on Principal Component Analysis and (b) histogram of particle size distribution of the sand assembly.

Table 2
Mean values of shape parameters from this study and Zheng et al. [57].

Sand	Sphericity	Roundness	Convexity	EI	FI
Ottawa-20/30 (this study)	0.93	0.82	0.97	0.86	0.87
Ottawa-20/30 (Zheng et al.)	0.96	0.76	–	0.80	–

these two parameters. However, there is a statistically significant deviation between 2D and 3D roundness and sphericity indexes for the sands. It demonstrates that quantifying non-spherical particle sphericity and roundness based on 2D projection images results in a different classification of particle morphology, compared with 3D results. The main reason for such a deviation can be explained as follows. Even though the maximum projection of particles shows the shortest and longest axes of particles, it can not provide information in the third direction. From this perspective, it is necessary to use 3D images to obtain accurate measures of roundness and sphericity.

Furthermore, the aspect ratios of all sand particles are plotted in Fig. 14(a). Notably, most particles fall into the category of "spheriod" with EI and FI greater than 2/3 on the basis of classification proposed by Zingg [59]. Fig. 14(b) shows the relationship between measured sphericity and convexity values. Most sand particles have sphericity and convexity values larger than 0.8. It is found that a strong correlation holds between the sphericity and convexity values, even though sphericity and convexity describe compactness from different perspectives.

4.3.3. Coordination number

Coordination number (CN) is an indicator of the particles' association with each other, which is one of the fundamental measurement revealing the structure (fabric) of a granular material. CN herein refers to the number of particles that are in contact with a certain particle. With regard to voxel-represented realistic particles, the contact between two particles is not always a point or a single continuous surface. Thus, identification of contact between particles involves analysis of the surface voxels of each particle in the sand assembly, that is, recognizing whether a particle of interest shares boundary voxels with its neighboring particles. Coordination number is calculated as the total number of unique neighboring particle IDs, which is the total number of particles in contact with the particle of interest. It is worth noting that the present approach may slightly overestimate the contact number due to the roughness of particle surface, especially for very angular or rough granular materials [9,60,61].

The distribution of CN for the sand assembly is plotted against that for the spherical and ellipsoidal packings in Fig. 15. The coordination number distributions of the spherical and ellipsoidal systems show significant differences from that of the sand assembly in shape and statistics. Specifically, the three packings have the same minimum CN of 3 but

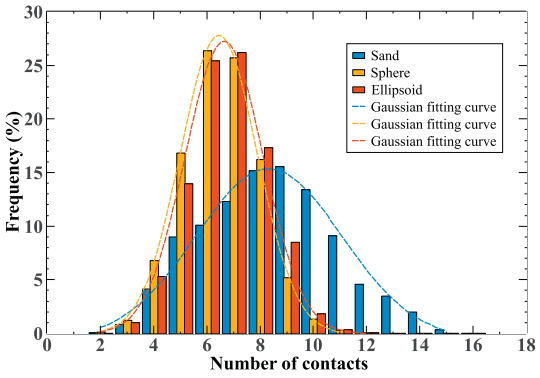

Fig. 15. Distribution of coordination number in sand, sphere and ellipsoid systems.

different maximum values (15, 12, 11 for the sand, ellipsoid and sphere assemblies, respectively). It suggests that a CN of 3 is the minimum for a frictional granular system to maintain an equilibrium state regardless of particle shape, while the maximum CN is significantly determined by particle shape. Furthermore, nearly 20% of the CN of sand particles is greater than 10, with an average CN of 8.39. In the sphere and ellipsoid packing systems, the average CN are 6.42 and 6.67, respectively, which are approximately identical. In general, natural sand has a greater CN than numerical packing of spheres and ellipsoids due to irregularity in particle shapes. The above observation also implies that the relationship between CN and packing density may be more complicated for realistic particle shapes, compared with the sphere and/or ellipsoid packings.

4.3.4. Contact network

Fig. 16 visualizes the connectivity with the ball-stick model for the three packings. For better effects of visualization, the particle volume has been scaled down to 30% of the original one, and inter-particle contacts are represented by sticks. It is clear that particle shape plays an important role in the particle connectivity and the distribution of coordination number. The contacts in the sands packing appear to be more intensive than the other two packings, which implies that sands have stronger connectivity than spheres and ellipsoids owing to the particle angularity.

We further analyzed the topological properties for each packing as an examination of the contact network. Topological distance of each single particle is introduced to capture the inter-particle connectivity. For a given particle, the particle topological distance between the particle and itself is assumed to be unity. The contact network at the next topological distance (i.e., $l = 2$) consists of all particles that are in contact with particles at the topological distance of unity. Following this manner, the topological distances of all particles within the entire packing can be measured. The procedure repeats for all particles, and the average

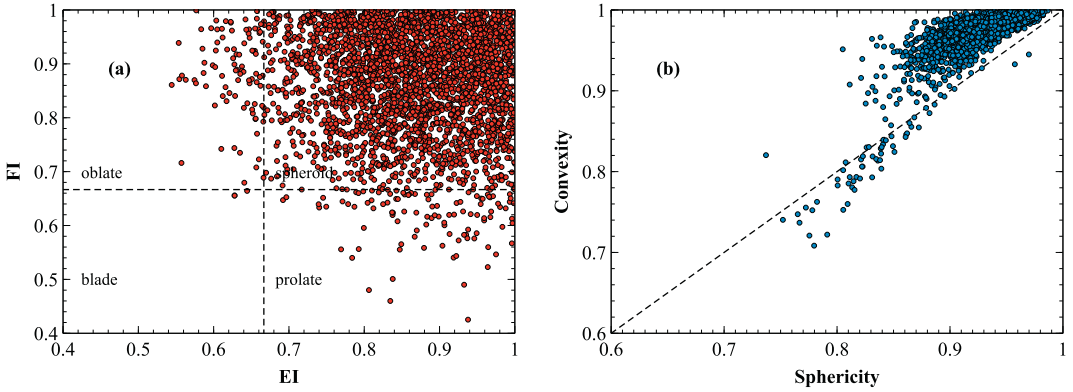

Fig. 14. Aspect ratios of sand particles (a) and relationship between sphericity and convexity (b).

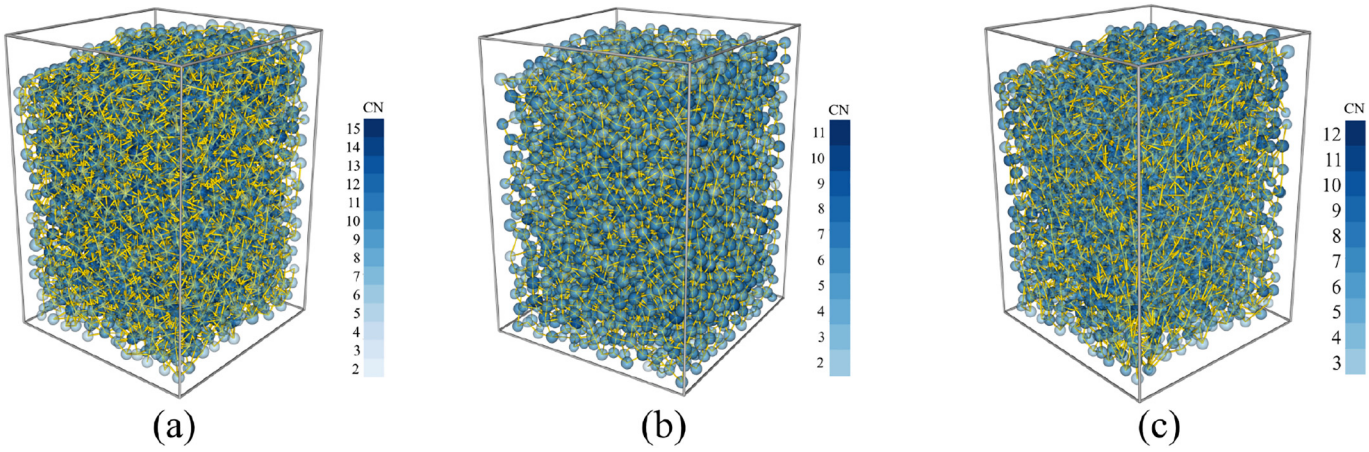

Fig. 16. Visualization of connectivity with the ball-stick model for the three packings: (a) sand, (b) sphere, (c) ellipsoid. The 'ball' (blue) represents each particle and the 'stick' (yellow) represents the contact between two particles. (For interpretation of the references to colour in this figure legend, the reader is referred to the web version of this article.)

number of particles N_c with different values of topological distance l is calculated accordingly.

Given that the packing is not an infinite, periodic structure with no boundaries (which is actually impossible for realistic packings), the present procedure does not start with a given 'central' particle. This procedure repeats on all particles so that each particle is calculated as the starting particle. Consequently, the boundary effect is mainly reflected in the maximum topological distance. The minimum value represents the average number of contacts of a given particle whereas the maximum value indicates that the topological distance reaches the boundary of the packing. Contact values between minimum and maximum topological distances represent the valid range of contact network.

Fig. 17 shows the average number of particles as a function of topological distance l for the three packings. It can be seen that the number of particles increases with topological distance until it reaches a certain maximum value above which the number of particles starts to decrease in the three packings. Notably, the average number of particles follows a quadratic relationship with the topological distance l. Besides, Besides, The maximum N_c appears at a topological distance l of 9. Furthermore, we fit the distribution function to the following equation for each packing

$$N_c = 3T_D l^2 + bl + c \tag{12}$$

where T_D is a descriptor of topological density and related to inter-particle connectivity, and a larger T_D corresponds to stronger inter-particle connectivity; b and c are fitted coefficients. The magnitude of T_D are 2.26, 1.43 and 1.11 for sand, sphere and ellipsoid packings, respectively, which indicates that the sand packing displays more significant connectivity than both sphere and ellipsoid packings when three packings possess the same global porosity. We note that the topological densities are consistently smaller than 10/3, which is the theoretical lower limit for Barlow packings [62].

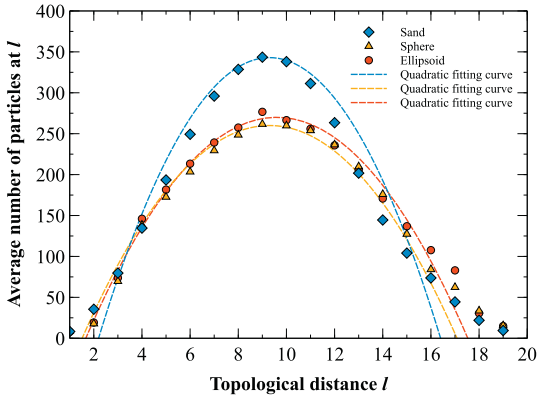

Fig. 17. Distribution of the average number of particles in contact with a given particle at different topological distances in sand, sphere and ellipsoid packings.

4.4. Void analysis

4.4.1. Voronoi cell morphological characteristics

The networks of Voronoi cells for the three packings are shown in Fig. 18, where a horizontal slice from each packing is cut out for an observational comparison. Fig. 19 exemplifies four neighboring Voronoi cells and the corresponding enclosed particles for each packing. It can be observed that a Voronoi cell encloses a particle with a similar morphological form to that of the particle, including orientations and sizes. Diverse morphological characteristics of Voronoi cells of different packings indicate that some volume or face related properties of Voronoi cells may be distinct. Hence, our analysis is focused on the Voronoi cell properties in the following work.

4.4.2. Local porosity

Porosity (or packing fraction) has been employed as a macroscopic variable to link with many characteristics of a granular material. In early studies, possible correlations between microscopic structure and packing fraction have been investigated for mono-disperse sphere packings, e.g., an invariant distribution in local volume [63]. Recently, such a universality has been comprehensively examined in the packings of polydisperse sphere and non-sphere systems regardless of initial states and loading conditions [35]. However, its validity remains to be verified for general granular materials with real amorphous particles, which are widely encountered in nature. Accordingly, we introduce local porosity n_l to examine the fluctuation of local volume which is defined as the ratio of the volume of the void to that of the Voronoi cell enclosing the given particle, given by

$$n_l = 1 - \frac{V_p}{V_v} \tag{13}$$

where V_v denotes the Voronoi cell volume. The average porosity ($\overline{n}$) of the sample is defined as $\overline{n} = \frac{1}{N}\sum_1^N n_l$, where N is the number of Voronoi cells. As pointed out by Bhatia et al. [64] and Alshibli [65], the average local porosity is not equal to the global porosity n_g for real soils. Nevertheless, with the uniqueness of Vornoi tessellation technique, the average porosity can be related to the global porosity in an implicit way, e.g., using the machine learning to bridge them. The distribution of local

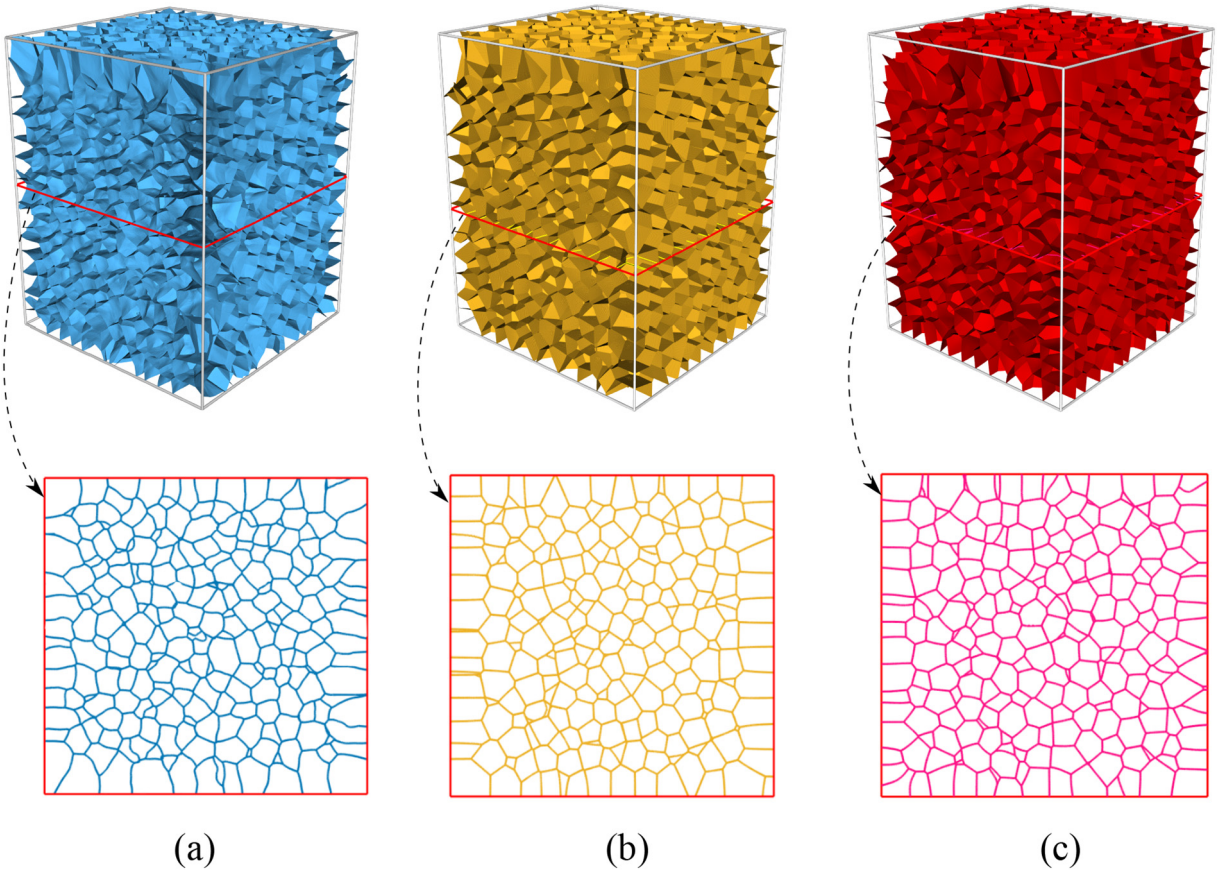

Fig. 18. Set Voronoi Tessellation for three systems (upper) with horizontal slices of Voronoi cells (lower): (a) sand, (b) sphere, and (c) ellipsoid, respectively.

porosity n_l (or local packing fraction $(1 - n_l)$) is an important topic in the context of a granular material [31,33,66]. The cumulative distribution functions (CDFs) of local porosity n_l are shown in Fig. 20(a). It can be seen that the statistical distributions of local porosity for the three packings present a similar pattern. According to the recent studies on the random packings of ellipsoids, cylinders, or superellipsoids [28,32,33,67], the probability distribution functions of the reduced local Voronoi cell volume follow Gaussian (or log-normal) distributions. Accordingly, we fit the probability distribution functions (PDFs) of n_l for the three packings by using a log-normal distribution, given by

$$\mathrm{PDF}(n_l) = \frac{1}{\tau\sqrt{2\pi}\cdot n_l}\exp\left(-\frac{(\ln(n_l)-\mu)^2}{2\tau^2}\right) \tag{14}$$

where μ and τ are geometrical parameters, representing the mean value and standard deviation of correlation distribution function, respectively. The mean values of local porosity $\overline{n}_l$ are 0.450, 0.462 and 0.441 for sand, sphere and ellipsoid systems, respectively. It can be seen that the local porosity for the realistic sands packing follows a log-normal distribution similar to the ideal-shaped particles, e.g., ellipsoids reported in [28]. Certain deviation of $\overline{n}_l$ among the three packings can also be observed,

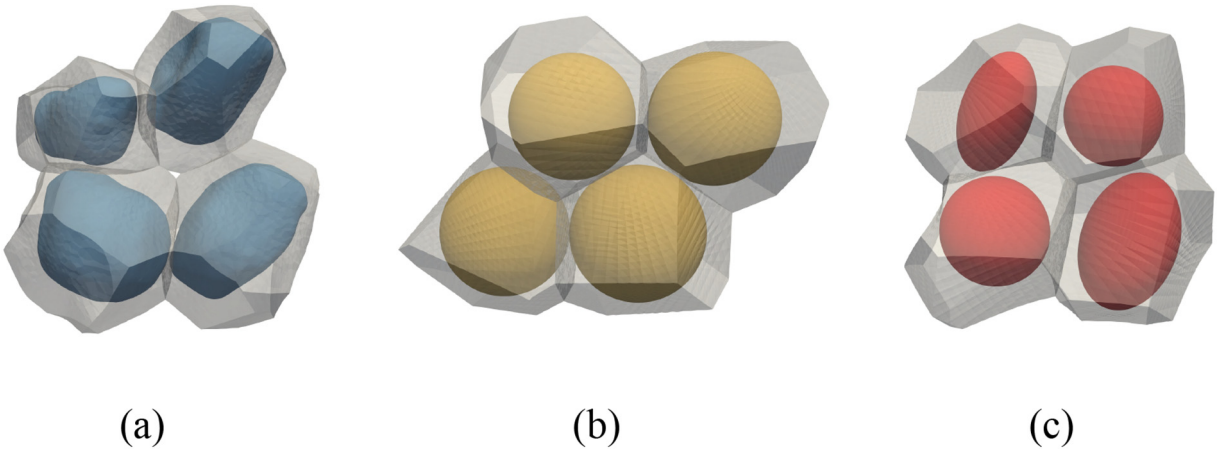

Fig. 19. Exemplified Voronoi cells enclosing extracted from the three systems: (a) sand, (b) sphere, and (c) ellipsoid.

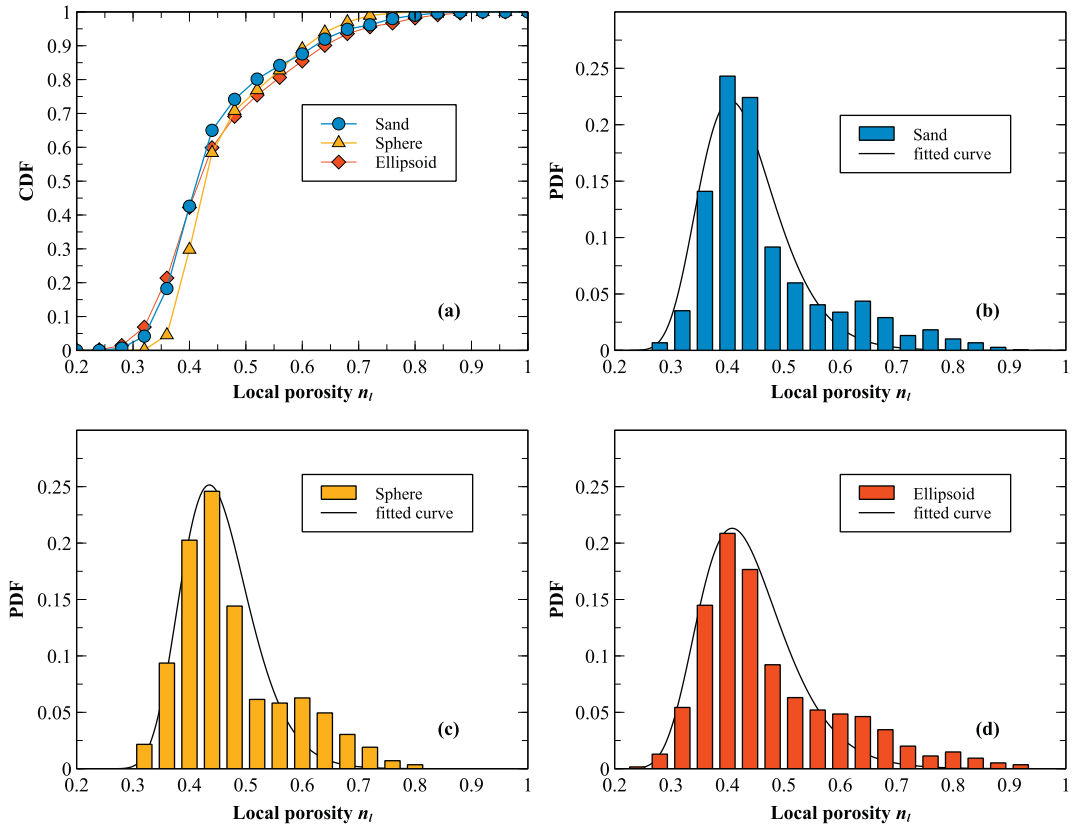

Fig. 20. Cumulative distributions (a) and probability distributions of local porosity of the three systems: (b) sand, (c) sphere and (d) ellipsoid.

which probably results from the difference in the particle shape since the global porosity and individual particle volumes are controlled. Previous studies show that there is a unique distribution of local volume for different packings with the same global porosity but different particle shapes [33,68], which may not be general enough for realistic complex shapes, at least for the case in this work.

4.4.3. Voronoi cell reduced surface area

Another significant dimensionless quantity of a Voronoi cell is reduced surface area S_r [69], which is defined as

$$S_r = 1 - \frac{S_p}{S_v} \tag{15}$$

where S_p and S_v are the surface area of a particle and the corresponding Voronoi cell, respectively. As shown in Fig. 21, similar to local porosity, S_r also presents a one-peak distribution with a slightly positive skewness for each packing. Thus, we find that their probability distributions can be described by the log-normal distribution function as well, given by

$$\mathrm{PDF}(S_r) = \frac{1}{\tau\sqrt{2\pi}\cdot S_r} \exp\left(-\frac{(\ln(S_r)-\mu)^2}{2\tau^2}\right) \tag{16}$$

The mean values of S_r we mainly focus on are 0.395, 0.516 and 0.381 for sand, sphere and ellipsoid systems, respectively. We notice that the differences in S_r between the three systems seem to be larger than that of the local porosity, which indicates that particle shape has a greater influence on the face related properties of Voronoi cells. Moreover, the surface area and local porosity of the ellipsoids and corresponding sand particles are slightly different in spite of the consistency of the aspect ratios (i.e. EI and FI), which might be associated to particle angularity. A further investigation on the details will be conducted in our future work.

5. Summary

This paper introduces a 3D Voronoi analysis framework to quantify the void spatial distribution within a granular packing composed of realistic grains. In the framework, we proposed an efficient and robust tool, PySVT, for Set Voronoi Tessellation, where either mathematically-expressed particles (e.g., poly-superellipsoids) or raw point-clouds from XCT reconstruction can be handled in parallel with a hybrid programming of Python and C++. It is worth noting that PySVT has the capability of handling a larger number of particles due to its specific parallelism.

A realistic assembly of Ottawa sand is reconstructed based on the XCT data. Due to the dual relationships between particles and voids, the characteristics of particles and their contact networks are examined at the microscopic scale with emphasis placed on particle size distribution, coordination number, contact network, and particle shape (aspect ratio, sphericity and convexity). To further investigate the effect of particle shape, another two numerical packings of spheres and ellipsoids are generated with the same global porosity as the realistic sand assembly by using SudoDEM (https://sudodem.github.io). With respect to contact network, a quadratic relationship between the average number of particles in contact with a given particle and the topological distance is obtained for the three systems. Furthermore, PySVT is utilized to tessellate these three packings, hereby yielding a triangulated representation of constructed Set Voronoi cells. A parametric analysis is conducted to evaluate the effect of local computational domain and Voronoi resolution on the results of SVT. It is found that a local domain consisting of approximately 60 particles and 2000 surface points per particle are reasonable for SVT of irregular particles by considering a trade-off

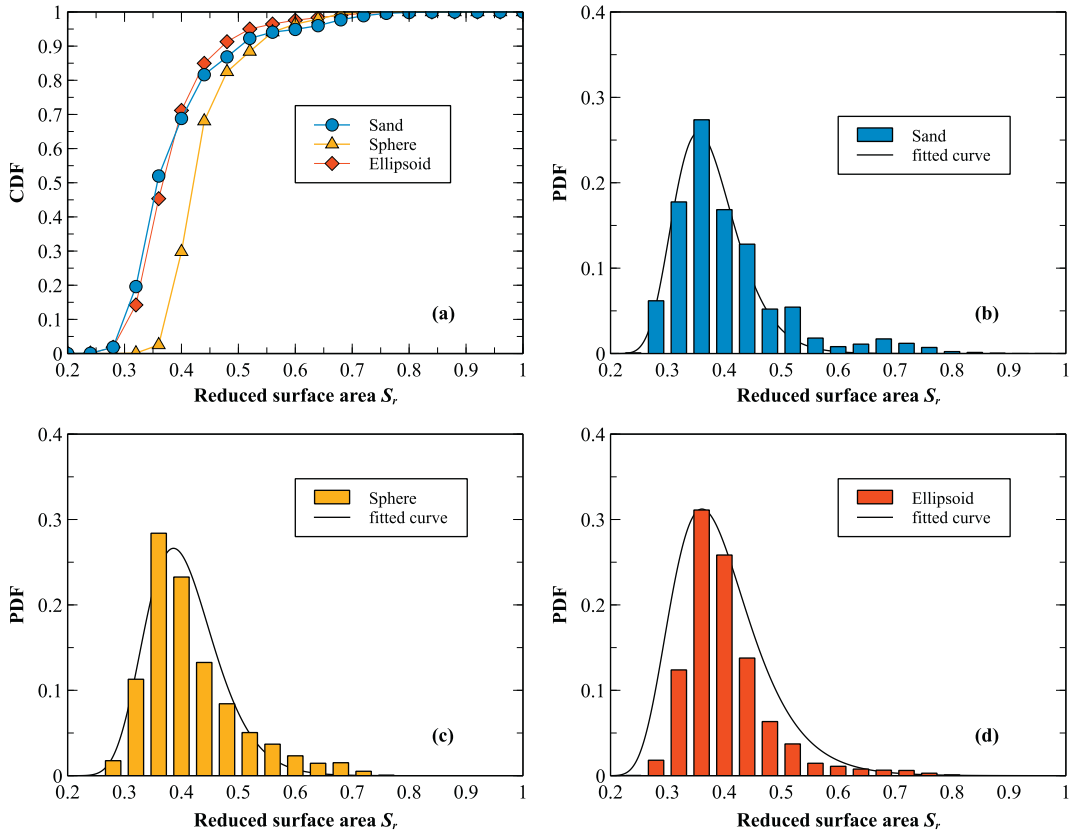

Fig. 21. Cumulative distributions (a) and probability distributions of reduced surface area of the three systems: (b) sand, (c) sphere and (d) ellipsoid.

between accuracy and efficiency. As for the properties of Voronoi cells, we focus on the local porosity and reduced surface area. Both local porosity and reduced surface area of Voronoi cells follow modified log-normal distributions for the three packings. The three packings possess almost the same global porosity, nevertheless, the local porosity and reduced surface area are more-or-less different between the systems because of the effect of angularity and aspect ratios. These findings should lead to a better understanding of the realistic grain packings and are helpful in guiding the exploration of microscopic characteristics.

Data availability statement

Source codes and data generated for the study are available from the authors upon request.

Declaration of Competing Interest

The authors declare that they have no known competing financial interests or personal relationships that could have appeared to influence the work reported in this paper.

Acknowledgment

This work was financially supported by the National Natural Science Foundation of China (by Project No. 51909095, No. 51679207 and No. 11972030), Guangdong Basic and Applied Basic Research Foundation (2020A1515011525), and the Fundamental Research Funds for Central Universities (D2192710). SZ would also thank the Hong Kong Scholars Program (2018). Any opinions, findings, and conclusions or recommendations expressed in this material are those of the authors and do not necessarily reflect the views of the financial bodies.

References

[1] S. Torquato, F.H. Stillinger, Jammed hard-particle packings: from kepler to bernal and beyond, Rev. Mod. Phys. 82 (2010) 2633–2672.
[2] O. Durán, N. Kruyt, S. Luding, Micro-mechanical analysis of deformation characteristics of three-dimensional granular materials, Int. J. Solids Struct. 47 (17) (2010) 2234–2245.
[3] G. Lu, J. Third, C. Müller, Discrete element models for non-spherical particle systems: from theoretical developments to applications, Chem. Eng. Sci. 127 (2015) 425–465.
[4] M. Oda, Initial fabrics and their relations to mechanical properties of granular material, Soils Found. 12 (1) (1972) 17–36.
[5] M. Oda, Fabrics and their effects on the deformation behaviors of sand, Special Report, 1976 1–59.
[6] J. Frost, C. Kuo, Automated determination of the distribution of local void ratio from digital images, Geotech. Test. J. 19 (2) (1996) 107–117.
[7] B. Zhou, J. Wang, Generation of a realistic 3D sand assembly using X-ray micro-computed tomography and spherical harmonic-based principal component analysis, Int. J. Numer. Anal. Methods Geomech. 41 (1) (2017) 93–109.
[8] R. Moreno-Atanasio, R.A. Williams, X. Jia, Combining X-ray microtomography with computer simulation for analysis of granular and porous materials, Particuology 8 (2) (2010) 81–99.
[9] A.M. Druckrey, K.A. Alshibli, R.I. Al-Raoush, 3D characterization of sand particle-to-particle contact and morphology, Comput. Geotech. 74 (2016) 26–35.
[10] Z. Cheng, J. Wang, Experimental investigation of inter-particle contact evolution of sheared granular materials using X-ray micro-tomography, Soils Found. 58 (6) (2018) 1492–1510.
[11] W. Fei, G.A. Narsilio, J.H. van der Linden, M.M. Disfani, Quantifying the impact of rigid interparticle structures on heat transfer in granular materials using networks, Int. J. Heat Mass Transf. 143 (2019) 118514.
[12] P.A. Cundall, O.D.L. Strack, A discrete numerical model for granular assemblies, Géotechnique 29 (1) (1979) 47–65.
[13] S. Zhao, N. Zhang, X. Zhou, L. Zhang, Particle shape effects on fabric of granular random packing, Powder Technol. 310 (2017) 175–186.
[14] T.-T. Ng, W. Zhou, G. Ma, X.-L. Chang, Macroscopic and microscopic behaviors of binary mixtures of different particle shapes and particle sizes, Int. J. Solids Struct. 135 (2018) 74–84.
[15] J. Nie, D. Li, Z. Cao, B. Zhou, A. Zhang, Probabilistic characterization and simulation of realistic particle shape based on sphere harmonic representation and nataf transformation, Powder Technol. 360 (2020) 209–220.
[16] B. Zhou, J. Wang, H. Wang, Three-dimensional sphericity, roundness and fractal dimension of sand particles, Géotechnique 68 (1) (2017) 18–30.

[17] L. Fan, J. Gao, Z. Wu, S. Yang, G. Ma, An investigation of thermal effects on micro-properties of granite by X-ray CT technique, Appl. Therm. Eng. 140 (2018) 505–519.
[18] A. Rachman, S. Anderson, C. Gantzer, Computed-tomographic measurement of soil macroporosity parameters as affected by stiff-stemmed grass hedges, Soil Sci. Soc. Am. J. 69 (5) (2005) 1609–1616.
[19] M. Naveed, S. Hamamoto, K. Kawamoto, T. Sakaki, M. Takahashi, T. Komatsu, P. Moldrup, M. Lamandé, D. Wildenschild, M. Prodanovic, et al., Correlating gas transport parameters and X-ray computed tomography measurements in porous media, Soil Sci. 178 (2) (2013) 60–68.
[20] K. Müller, S. Katuwal, I. Young, M. McLeod, P. Moldrup, L.W. De Jonge, B. Clothier, Characterising and linking X-ray CT derived macroporosity parameters to infiltration in soils with contrasting structures, Geoderma 313 (2018) 82–91.
[21] M.S. Rahner, M. Halisch, C.P. Fernandes, A. Weller, V.S.S. dos Santos, Fractal dimensions of pore spaces in unconventional reservoir rocks using X-ray nano-and micro-computed tomography, J. Nat. Gas. Sci. Eng. 55 (2018) 298–311.
[22] N. Elyeznasni, F. Sellami, V. Pot, P. Benoit, L. Vieublé-Gonod, I. Young, S. Peth, Exploration of soil micromorphology to identify coarse-sized om assemblages in X-ray CT images of undisturbed cultivated soil cores, Geoderma. 179 (2012) 38–45.
[23] R.K. Sahoo, S.K. Singh, B. Mishra, Surface and bulk 3D analysis of natural and processed ruby using electron probe micro analyzer and X-ray micro CT scan, J. Electron Spectrosc. Relat. Phenom. 211 (2016) 55–63.
[24] N. Nunan, K. Ritz, M. Rivers, D.S. Feeney, I.M. Young, Investigating microbial micro-habitat structure using X-ray computed tomography, Geoderma. 133 (3–4) (2006) 398–407.
[25] S. Hamamoto, P. Moldrup, K. Kawamoto, T. Sakaki, T. Nishimura, T. Komatsu, Pore network structure linked by X-ray CT to particle characteristics and transport parameters, Soils Found. 56 (4) (2016) 676–690.
[26] H. Dong, M.J. Blunt, Pore-network extraction from micro-computerized-tomography images, Phys. Rev. E 80 (3) (2009), 036307, .
[27] R. Al-Raoush, C. Willson, Extraction of physically realistic pore network properties from three-dimensional synchrotron X-ray microtomography images of unconsolidated porous media systems, J. Hydrol. 300 (1–4) (2005) 44–64.
[28] S. Zhao, T.M. Evans, X. Zhou, Three-dimensional Voronoi analysis of monodisperse ellipsoids during triaxial shear, Powder Technol. 323 (2018) 323–336.
[29] A. Baule, R. Mari, L. Bo, L. Portal, H.A. Makse, Mean-field theory of random close packings of axisymmetric particles, Nat. Commun. 4 (2013) 2194.
[30] L. Yi, K. Dong, R. Zou, A. Yu, Radical tessellation of the packing of spheres with a log-normal size distribution, Phys. Rev. E 92 (3) (2015), 032201, .
[31] K.A. Newhall, I. Jorjadze, E. Vanden-Eijnden, J. Brujic, A statistical mechanics framework captures the packing of monodisperse particles, Soft Matter 7 (24) (2011) 11518–11525.
[32] K. Dong, C. Wang, A. Yu, Voronoi analysis of the packings of non-spherical particles, Chem. Eng. Sci. 153 (2016) 330–343.
[33] F.M. Schaller, M. Neudecker, M. Saadatfar, G.W. Delaney, G.E. Schröder-Turk, M. Schröter, Local origin of global contact numbers in frictional ellipsoid packings, Phys. Rev. Lett. 114 (15) (2015) 158001.
[34] G.E. Schröder-Turk, W. Mickel, S.C. Kapfer, M.A. Klatt, F.M. Schaller, M.J. Hoffmann, N. Kleppmann, P. Armstrong, A. Inayat, D. Hug, et al., Minkowski tensor shape analysis of cellular, granular and porous structures, Adv. Mater. 23 (22−23) (2011) 2535–2553.
[35] S. Zhao, J. Zhao, N. Guo, Universality of internal structure characteristics in granular media under shear, Phys. Rev. E 101 (1) (2020), 012906, .
[36] A.C. Kak, M. Slaney, G. Wang, Principles of computerized tomographic imaging, Med. Phys. 29 (1) (2002), https://doi.org/10.1118/1.1455742.
[37] J.C. Russ, The Image Processing Handbook, CRC press, 2006.
[38] N. Otsu, A Threshold Selection Method From Gray-Level Histograms, 9, IEEE transactions on systems, man, and cybernetics, 1979 62–66 (1).
[39] C.T. Rueden, J. Schindelin, M.C. Hiner, B.E. DeZonia, A.E. Walter, E.T. Arena, K.W. Eliceiri, Imagej2: imagej for the next generation of scientific image data, BMC. Bioinforma. 18 (1) (2017) 529.
[40] Y. Wang, C. Lin, J. Miller, 3D image segmentation for analysis of multisize particles in a packed particle bed, Powder Technol. 301 (2016) 160–168.
[41] M. Kazhdan, H. Hoppe, Screened poisson surface reconstruction, ACM. Trans. Gr. (ToG). 32 (3) (2013) 1–13.
[42] F. Aurenhammer, Power diagrams: properties, algorithms and applications, SIAM J. Comput. 16 (1) (1987) 78–96.
[43] F.M. Schaller, S.C. Kapfer, M.E. Evans, M.J. Hoffmann, T. Aste, M. Saadatfar, K. Mecke, G.W. Delaney, G.E. Schröder-Turk, Set Voronoi diagrams of 3D assemblies of aspherical particles, Philos. Mag. 93 (31−33) (2013) 3993–4017.
[44] A. Shapiro, Monte carlo sampling methods, Handbooks in Operations Research and Management Science, 10, 2003, pp. 353–425.
[45] D. Mirri, G. Iuculano, A. Menchetti, F. Filicori, M. Catelani, Recursive Random Sampling Strategy for a Digital Wattmeter, in: [1992], Conference Record IEEE Instrumentation and Measurement Technology Conference, IEEE, 1992 577–582.
[46] R. Bridson, Fast Poisson Disk Sampling in Arbitrary Dimensions, in: ACM SIGGRAPH 2007 Sketches, Association for Computing Machinery, New York, NY, USA, 2007 22 es.
[47] M. Corsini, P. Cignoni, R. Scopigno, Efficient and flexible sampling with blue noise properties of triangular meshes, IEEE Trans. Vis. Comput. Graph. 18 (2012) 914–924.
[48] L.Y. Wei, Parallel poisson disk sampling, ACM Trans. Graph. 27 (3) (2008) 1–9.
[49] C. Rycroft, Voro++: A Three-Dimensional Voronoi Cell Library in C++, Tech. Rep, Lawrence Berkeley National Lab.(LBNL), Berkeley, CA (United States), 2009.
[50] S. Zhao, X. Zhou, Effects of particle asphericity on the macro-and micro-mechanical behaviors of granular assemblies, Granul. Matter 19 (2) (2017) 38.
[51] S. Zhao, T. Evans, X. Zhou, Effects of curvature-related dem contact model on the macro-and micro-mechanical behaviours of granular soils, Géotechnique 68 (12) (2018) 1085–1098.
[52] V. Cnudde, M.N. Boone, High-resolution x-ray computed tomography in geosciences: a review of the current technology and applications, Earth Sci. Rev. 123 (2013) 1–17.
[53] C.S. Willson, N. Lu, W.J. Likos, Quantification of grain, pore, and fluid microstructure of unsaturated sand from x-ray computed tomography images, Geotech. Test. J. 35 (6) (2012) 911–923.
[54] E.J. Garboczi, J.W. Bullard, 3d analytical mathematical models of random star-shape particles via a combination of x-ray computed microtomography and spherical harmonic analysis, Adv. Powder Technol. 28 (2) (2017) 325–339.
[55] S. Blott, K. Pye, Particle shape: a review and new methods of characterization and classification, Sedimentology 55 (1) (2008) 31–63.
[56] H. Wadell, Volume, shape, and roundness of rock particles, J. Geol. 40 (5) (1932) 443–451.
[57] J. Zheng, R.D. Hryciw, Roundness and sphericity of soil particles in assemblies by computational geometry, J. Comput. Civ. Eng. 30 (6) (2016), 04016021, .
[58] B. Zhao, J. Wang, 3D quantitative shape analysis on form, roundness, and compactness with μCT, Powder Technol. 291 (2016) 262–275.
[59] T. Zingg, Beitrag Zur Schotteranalyse, Ph.D. thesis ETH Zurich, 1935.
[60] L. Olmos, J.-M. Chaix, S. Nadler, O. Bonnefoy, J.-L. Gelet, G. Thomas, Study by X-ray microtomography of the horizontal vibration effects on sand densification, Granul. Matter 18 (3) (2016) 61.
[61] F.H. Kim, D. Penumadu, J. Gregor, M. Marsh, N. Kardjilov, I. Manke, Characterizing partially saturated compacted-sand specimen using 3D image registration of high-resolution neutron and X-ray tomography, J. Comput. Civ. Eng. 29 (6) (2015), 04014096, .
[62] J.H. Conway, N.J. Sloane, Low–dimensional lattices. vii. coordination sequences, Proc R Soc Lond. Ser A: Math, Phys Eng Sci. 453 (1966) (1997) 2369–2389.
[63] T. Aste, T. Di Matteo, M. Saadatfar, T.J. Senden, M. Schröter, H.L. Swinney, An invariant distribution in static granular media, EPL (Europhys Lett) 79 (2) (2007) 24003.
[64] S.K. Bhatia, A.F. Soliman, Frequency distribution of void ratio of granular materials determined by an image analyzer, Soils Found. 30 (1) (1990) 1–16.
[65] K.A. Alshibli, H.A. El-Saidany, Quantifying void ratio in granular materials using Voronoi tessellation, J. Comput. Civ. Eng. 15 (3) (2001) 232–238.
[66] K.A. Newhall, I. Jorjadze, E. Vanden-Eijnden, J. Brujic, A Granocentric Model Captures the Statistical Properties of Monodisperse Random Packings, arXiv preprint arXiv: 1202.0834 2012.
[67] L. Liu, Z. Yu, W. Jin, Y. Yuan, S. Li, Uniform and decoupled shape effects on the maximally dense random packings of hard superellipsoids, Powder Technol. 338 (2018) 67–78.
[68] C. Xia, K. Zhu, Y. Cao, H. Sun, B. Kou, Y. Wang, X-ray tomography study of the random packing structure of ellipsoids, Soft Matter 10 (7) (2014) 990–996.
[69] R. Yang, R. Zou, A. Yu, Voronoi tessellation of the packing of fine uniform spheres, Phys. Rev. E 65 (4) (2002), 041302, .
[70] S. Zhao, J. Zhao, *SudoDEM* : Unleashing the predictive power of the discrete element method on simulation for non-spherical granular particles, Computer Physics Communications (2020), https://doi.org/10.1016/j.cpc.2020.107670.